4

# Modeling of a One Flexible Link Manipulator

Mohamad Saad
*Department of Applied Sciences*
*Université du Québec en Abitibi-Témiscamingue*
*Rouyn-Noranda, Québec, Canada*
*mohamad.saad@uqat.ca*

## 1. Introduction

Dynamics and control of flexible robot manipulators have received wider attention during the last two decades. In manufacturing and space applications, the use of lightweight structures in robot manipulators is motivated by their capacity for high speed maneuvers, their high payload to arm weight ratio, higher mobility, reduced energy consumption, and lower inertia forces for accurate positioning. To insure satisfactory performances of such systems, their flexibility should be included in modeling and in control design. This flexibility becomes more significant in cases of larger structures and more stringent performance demands.
In modeling flexible link manipulators, the most widely used methods to generate spatially discrete models are the Assumed-Mode Method (AMM), and the Finite Element Method (FEM). The accuracy of the dynamical model obtained from the analytical formulation is highly dependent on the adopted mode shapes of the link deflection and their number.
In the AMM, the shape functions are typically eigenfunctions of a closely related simpler problem with standard boundary conditions (BCs). For example, the Euler-Bernoulli beam in one of the following configurations (Mirovitch, 1967): clamped-free, pinned-free, clamped-mass, or pinned-mass. In the FEM, the shape functions, known as interpolation functions, are simple polynomials that verify the continuity conditions between two adjacent elements or nodes. Examples of interpolation functions are Hermite cubics (Chen & Menq, 1990), cubic splines (Cho et al., 1991; Saad et al., 2006) and cubic B-splines (Saad et al., 2006).
In the literature, most of the comparison studies that have been done are for clamped versus pinned mode shapes (Barbieri & Ozguner, 1988; Cetinkunt & Yu, 1991; Hastings and Book, 1987). The general conclusion is that for a slewing beam, clamped modes are more appropriate than pinned modes. Meirovitch and Kwak (Mirovitch & Kwak, 1990) compared the convergence rate of a clamped-free assumed-mode model vs. a linear interpolation finite elements model in estimating the frequencies of a horizontal beam with longitudinal deformation. The convergence rate was slow in both cases. To accelerate the rate of convergence, assumed-modes that take into account the natural BCs and interpolation functions that have the ability to satisfy the differential equation of the system were introduced. Buffinton and Lam (Buffinton & Lam, 1992) compared a lumped-parameter model versus an AMM in modeling and control of a one-link flexible manipulator in the horizontal plane. They concluded that from a control viewpoint, the AMM based model yields better performances when compared to lumped-parameter model. In comparing two clamped-mass assumed-modes and two Hermite cubic finite elements, Theodore and Ghosal (Theodore & Ghosal, 1995) concluded that

fewer mathematical operations are required for inertia matrix computation with the finite element model in comparison with the assumed-modes formulation. However, the number of equations of motion is greater for the finite element model. Junkins and Kim (Junkins & Kim, 1993) found that, for a flexible appendage with rigid body motion, the convergence rate of the natural frequencies of clamped-free assumed-modes is much slower than the convergence rate of Hermite cubic finite elements. This is because the shape functions used in the AMM satisfy only the essential BCs of the given problem. Tokhi and Mohamed (Tokhi & Mohamed, 1999) evaluated the computational requirements of FEM in characterizing the behavior of a flexible link. They compared the convergence rate of the first three frequencies while increasing the number of elements. In contrast with most studies, the frequencies were under-estimated because the model did not include the base and load inertias.
Parametric and simulation studies were also performed to investigate the influence of different system parameters on the natural frequencies (Li et al., 1998) or on the zeros and the poles of the transfer functions of a flexible link (Parks & Pak, 1991). To validate the models of multi-link flexible manipulators, experimental frequency response results are generally compared to linearized model responses (Nicosia et al., 1996) or to simplified model responses (Book & Obergfell, 2000; Stanway et al., 1998). A reduced finite element model is used in (Xia & Menq, 1992) to study the effect of robot configurations on the elastic mode shape functions.
In control design, the issue of the number of flexible modes used becomes important, especially when using the mass matrix in the control law. As the number of modal variables is increased in the model, more elastic modes can be obtained and more accurate estimation of the dominant modes of the system can be achieved. However, the computational burden makes dynamical simulations and control very difficult (Xia & Menq, 1992). In particular, the mass matrix becomes more ill-conditioned. This can lead to loss of performance or even instability (Moallem et al., 2002). A trade-off is often required between model accuracy and avoiding the loss of reliability due to increased numerical ill-conditioning that is inherent to using a large number of flexible modes.
These studies show the importance of a good representation of the flexibility in order to get an accurate and precise model and point to the lack of systematic methods to determine the appropriate choice of shape functions or their number. Two important questions come to mind in particular: does the convergence rate of the eigenfrequencies represent a good performance index ? How accurately do different choices of shape functions represent the eigenmodes of a flexible link ?
The objective of this work is to develop the dynamical model of one flexible link under the assumption of small deformations using Lagrange equations and takng into account the foreshortening effect of the link. A compact dynamical model is given for different shape functions. The orthogonality relations between shape functions are presented. The objective is also to compare the performance of the different shape functions with respect to their ability to accurately represent the dynamic and the static behavior of a flexible rotating beam system. Based on the mathematical model of this system, an analytical solution for the exact shape functions describing the link's flexibility is developed. These functions are then substituted in the spatially discrete model to obtain a reference model with ideal performances for all cases presented in the following sections. Therefore, the performances of the different shape functions based models are compared to the reference one.
Several candidates based on the AMM and FEM are selected to develop the approximated models. In this paper, however, the FEM is not used in the formal sense. The interpolation functions are generated locally for an element but are represented globally over the entire

length of the link. This representation allows the use of locally defined functions in the AMM as will be seen in the sequel. The selected shape functions are: the eigenfunctions of a beam rotating in the horizontal plane, a clamped-payload beam, and a clamped-free beam, together with the polynomial functions, the cubic splines, and the cubic B-splines. The comparison is done for the eigenfrequencies, the eigenmodes and their derivatives, and for the static deformation under gravity. The second derivatives are particularly important because they are related to the link curvature. The latter is widely used in modeling and control experiments to measure and estimate flexibility using strain gauges (Piedboeuf & Miller, 1994). In addition, load parameters are changed from their nominal values to test sensitivity of the shape functions based models. In all cases, we assume that the beam parameters are well known.
Section 2 describes the features of the flexible link under consideration and presents the continuous model of this system. The eigenvalues problem and the discretized model are presented in sections 3 and 4 respectively. Section 5 deals with the analytical aspects of the shape functions. A comparison of the different assumed-modes is presented in Section 6 in which the merits and demerits of each shape function are examined.

## 2. The Continuous Model

Figure 1 shows the test bed system. It consists of a motor, a flexible beam, and a payload. The system parameters and their nominal values are given in Table 1. The motor applied

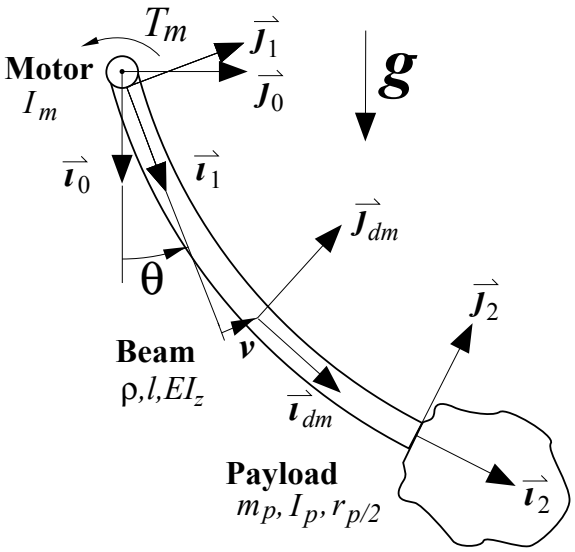


Fig. 1. A flexible rotating beam

torque is $T_m$. Gravity acts along the $x$-axis of frame $(\vec{\imath}_0, \vec{j}_0)$. The motor angular position is $\theta(t)$ and the link deformation is $v(x,t)$. For simplification, $x$ and $t$ are omitted. When writing the dynamical equations, we make the following assumptions. The flexible link is modeled as a Euler-Bernoulli beam and the deformation is assumed to be small. We also take into account the foreshortening effect of the link by assuming a second order kinematic. However, when comparing the assumed modes models, we eliminate the foreshortening effect by assuming

| Parameter Name | | Nominal Value |
|---|---|---|
| Motor inertia | $(I_m)$ | $10\ kg\ m^2$ |
| Beam length | $(l)$ | $1.4\ m$ |
| Beam linear density | $(\rho)$ | $1\ kg/m$ |
| Beam rigidity | $(EI_z)$ | $500\ N\ m^2$ |
| Payload mass | $(m_p)$ | $2\ kg$ |
| Payload inertia | $(I_p)$ | $0.36\ kg\ m^2$ |
| Payload center of mass | $(r_p)$ | $0\ m$ |

Table 1. Nominal parameters.

small motor angular velocity and by linearizing the dynamical equations at the motor position $\theta = \pi/2$. The joint and the beam internal damping are neglected.
The continuous model consists of one ordinary differential equation (ODE) for the motor's motion, and a partial differential equation (PDE) with four associated boundary conditions (BCs) for the flexible link.

### 2.1 Kinematics

The position of reference frame $\mathcal{R}_1$ relative to the inertial reference system $\mathcal{R}_0$ is:

$$^0P_1 = \begin{bmatrix} 0 & 0 & 0 \end{bmatrix}^T$$

The rotation matrix of $\mathcal{R}_1$ relative to $\mathcal{R}_0$ is :

$$^0R_1 = \begin{bmatrix} \cos\theta & -\sin\theta & 0 \\ \sin\theta & \cos\theta & 0 \\ 0 & 0 & 1 \end{bmatrix}$$

Let $dm$ be an element of the link with $x$ is the distance from the base along the link's neutral axis, $\vec{\imath}_1$. The position of $\mathcal{R}_{dm}$ relative to $\mathcal{R}_1$ is:

$$^1P_{dm} = \begin{bmatrix} x - \underbrace{\frac{1}{2}\int_0^x v'^2(s,t)ds}_{\mathcal{O}_2(v)} \\ v(x,t) \\ 0 \end{bmatrix}^T$$

The $\mathcal{O}_2(v)$ term is a 2nd order term in $v$. This term is to be neglected if first order kinematic was considered. The rotation matrix of $\mathcal{R}_{dm}$ relative to $\mathcal{R}_1$ is (Piedboeuf, 1998):

$$^1R_{dm} = \begin{bmatrix} 1 - \frac{1}{2}v'^2 & -v' & 0 \\ v' & 1 - \frac{1}{2}v'^2 & 0 \\ 0 & 0 & 1 \end{bmatrix}$$

Note that $^1R_{dm}$ verify the following: $^1R_{dm}\ ^1R_{dm}^T = I$, where $I$ is the identity matrix.

The position vector of the payload center of mass relative to $\mathcal{R}_1$ is:

$$\begin{aligned} {}^1P_c &= {}^1P_2 + {}^1R_2\,{}^2P_c \\ &= \begin{bmatrix} L + r_p + -\frac{1}{2}\int_0^L v'^2 dx - \frac{1}{2} r_p\, v'^2_L \\ v_L + r_p\, v'_L \\ 0 \end{bmatrix} \end{aligned}$$

The ${}^1R_2$ matrix is obtained from ${}^1R_{dm}$ by substituting $x$ by $L$. If the payload is concentrated at the links extremity, $r_c = 0$. The rotation matrix of the payload center of mass relative to $\mathcal{R}_1$ is:

$${}^1R_c = {}^1R_2\,{}^2R_c = \begin{bmatrix} 1 - \frac{1}{2}v'^2_L & -v'_L & 0 \\ v'_L & 1 - \frac{1}{2}v'^2_L & 0 \\ 0 & 0 & 1 \end{bmatrix}$$

where ${}^2R_c$ is the identity matrix.
The angular velocity of $\mathcal{R}_1$ relative to $\mathcal{R}_0$ is:

$$\omega_1 = \dot{\theta}\,\vec{k}_1$$

Using the antisymmetric matrix to represent the velocity of an element $dm$ of the link:

$$S = {}^1\dot{R}_{dm}\,{}^1R_{dm}^{-1} = \begin{bmatrix} 0 & -\dot{v}' & 0 \\ \dot{v}' & 0 & 0 \\ 0 & 0 & 0 \end{bmatrix} = \begin{bmatrix} 0 & -\omega_z & \omega_y \\ \omega_z & 0 & -\omega_x \\ -\omega_y & \omega_x & 0 \end{bmatrix}$$

the angular velocity of $\mathcal{R}_{dm}$ relative to $\mathcal{R}_1$ is then given by:

$${}^1\Omega_{dm} = \begin{bmatrix} \omega_x \\ \omega_y \\ \omega_z \end{bmatrix} = \begin{bmatrix} 0 \\ 0 \\ \dot{v}' \end{bmatrix}$$

and relative to $\mathcal{R}_0$, it is given by:

$$\omega_{dm} = \omega_1 + {}^0R_1\,{}^1\Omega_{dm} = \begin{bmatrix} 0 & 0 & \dot{\theta} + \dot{v}' \end{bmatrix}^T$$

The linear velocity of the origin of $\mathcal{R}_{dm}$ relative to $\mathcal{R}_0$ is:

$$v_{dm} = {}^0R_1\,{}^1V_{dm} + \omega_1 \times ({}^0R_1\,{}^1P_{dm})$$

When expressed in $\mathcal{R}_1$, it becomes:

$$\begin{aligned} {}^1v_{dm} &= {}^0R_1^T\, v_{dm} = \frac{d\,{}^1P_{dm}}{dt} + \omega_1 \times {}^1P_{dm} \\ &= \begin{bmatrix} -\dot{\theta}\, v \\ \dot{v} + x\dot{\theta} \\ 0 \end{bmatrix} + \begin{bmatrix} -\int_0^x v'\,\dot{v}'ds \\ -\frac{1}{2}\dot{\theta}\int_0^x v'^2\,ds \\ 0 \end{bmatrix} \end{aligned}$$

The payload angular velocity is obtained from $\omega_{dm}$ by replacing $x$ by $L$:

$$\omega_c = \begin{bmatrix} 0 & 0 & \dot{\theta} + \dot{v}'_L \end{bmatrix}^T$$

The absolute velocity of the payload, written in $\mathcal{R}_1$, is:

$$\begin{aligned} {}^1v_c &= \frac{d}{dt}({}^1P_c) + \omega_1 \times {}^1P_c \\ &= \begin{bmatrix} -\dot\theta(v_L + r_p\, v'_L) - \int_0^L v'\,\dot v'\,dx - r_p\, v'_L\,\dot v'_L \\ (L+r_p)\dot\theta + \dot v_L + r_p\,\dot v'_L - \frac{1}{2}\dot\theta\int_0^L v'^2\,dx - \frac{1}{2}r_p\,\dot\theta\, v'^2_L \\ 0 \end{bmatrix} \end{aligned}$$

The gravity vector is represented in $\mathcal{R}_0$ by:

$${}^0g = \begin{bmatrix} g & 0 & 0 \end{bmatrix}^T$$

where $g$ is the gravitational acceleration. In $\mathcal{R}_1$, it is given by

$${}^1g = {}^1R_0\,{}^0g = {}^0R_1^T\,{}^0g = \begin{bmatrix} g\cos\theta \\ -g\sin\theta \\ 0 \end{bmatrix}$$

### 2.2 Kinetic Energy

The kinetic energy of the given system is given by:

$$T = T_B + \int_0^L T_{dm} + T_C \tag{1}$$

where $T_B$ is the kinetic energy of the base,

$$T_B = \frac{1}{2} I_m\,\dot\theta^2$$

$T_{dm}$ is the kinetic energy of an element of the link,

$$T_{dm} = \frac{1}{2}\rho\, v_{dm}^T\, v_{dm}\, dx = \frac{1}{2}\rho\,{}^1v_{dm}^T\,{}^1v_{dm}\, dx$$

and $T_C$ is the kinetic energy of the payload,

$$T_C = \frac{1}{2} I_p\,\omega_c^2 + \frac{1}{2} M_p\, v_c^T\, v_c = \frac{1}{2} I_p\,\omega_c^2 + \frac{1}{2} M_p\,{}^1v_c^T\,{}^1v_c$$

(See Appendix for kinetic energy expressions).
Linearizing the kinetic energy to the 2nd order in in $v$ give:

$$\begin{aligned} T = {} & \frac{1}{2}\left(I_m + \frac{1}{3}\rho\, L^3 + I_p + M_p(L+r_p)^2\right)\dot\theta^2 \\ & + \dot\theta\left(\rho\int_0^L x\,\dot v\,dx + M_p(L+r_p)\dot v_L + [I_p + M_p\, r_p(L+r_p)]\dot v'_L\right) \\ & + \frac{1}{2}\rho\int_0^L \dot v^2\,dx + \frac{1}{2}M_p\dot v_L^2 + \frac{1}{2}(I_p + M_p\, r_p^2)\dot v'^2_L + M_p\, r_p\dot v_L\,\dot v'_L \\ & + \frac{1}{2}\dot\theta^2\left(\rho\int_0^L v^2\,dx + M_p\, v_L^2 + 2M_p\, r_p\, v_L\, v'_L\right) \\ & - \frac{1}{2}\dot\theta^2\left(\rho\int_0^L x\int_0^x v'^2\,ds + M_p(L+r_p)\int_0^L v'^2\,dx\right) - \frac{1}{2}\dot\theta^2\left(M_p\, r_p\, L v'^2_L\right) \end{aligned} \tag{2}$$

### 2.3 Potential Energy

The potential energy of the given system is given by:

$$V = \int_0^L V_{dm} + V_c \tag{3}$$

where $V_{dm}$ is the potential energy of the links element $dm$,

$$\begin{aligned} V_{dm} &= \frac{1}{2} E I_z \, v''^2 \, dx - \rho \, {}^1g^T \, {}^1P_{dm} \, dx \\ &= \frac{1}{2} E I_z \, v''^2 \, dx - \rho \, g \, x \, \cos\theta \, dx + \rho \, g \, v \sin\theta \, dx + \frac{1}{2} \rho \, g \, \cos\theta \int_0^x v'^2 ds dx \end{aligned}$$

and $V_c$ is the potential energy of the payload:

$$\begin{aligned} V_c &= -M_p \, {}^1g^T \, {}^1P_c \\ &= -M_p \, g (L + r_p) \cos\theta + M_p \, g \, (v_L + r_p v'_L) \sin\theta + \frac{1}{2} M_p \, g \cos\theta \left( \int_0^L v'^2 dx + r_p \, v'^2_L \right) \end{aligned}$$

### 2.4 Rayleigh Dissipation Function

Friction is due to the motor's viscous friction and the link's internal damping. The Rayleigh dissipation function is then given by:

$$R = \frac{1}{2} b_m \dot{\theta}^2 + \frac{1}{2} k_e E I_z \int_0^L \dot{v}''^2 \, dx \tag{4}$$

where $k_e$ is the links internal damping coefficient.

### 2.5 Dynamics

To develop the dynamics of the given system, we use Hamilton's principle associated with the kinetic and potential energy developed previously. The variational of these expressions are simplified using integration by parts. First we neglect damping forces. The only non conservative applied force is the motor torque $T_m$. Two dynamic equations are then obtained. The first one is associated with the motor's angle $\theta$, and the second is associated with the deformation of the link $v$. Moreover, four boundary conditions (BCs) are associated to the dynamic equation of the deformation. These conditions describe the way in which the arm is attached to the base (geometrical BCs) and to the payload (natural BCs).
In the absence of viscous friction, the dynamic equation associated with $\theta$ is:

$$\begin{aligned} T_m &= \left( I_m + \frac{1}{3} \rho \, L^3 + I_p + M_p (L + r_p)^2 \right) \ddot{\theta} + \int_0^L \rho \, x \, \ddot{v} \, dx + M_p (L + r_p) \ddot{v}_L \\ &\quad + (I_p + M_p \, r_p (L + r_p)) \ddot{v}'_L + \left( \frac{1}{2} \rho \, g \, L^2 + M_p \, g \, (L + r_p) \right) \sin\theta \\ &\quad + \left[ \int_0^L \rho \, g \, v dx + M_p \, g \, (v_L + r_p \, v'_L) \right] \cos\theta + \rho \int_0^L \frac{\partial}{\partial t} (\dot{\theta} \, v^2) \, dx \\ &\quad - \frac{1}{2} \rho \int_0^L (L^2 - x^2) \frac{\partial}{\partial t} (\dot{\theta} \, v'^2) \, dx + M_p \, \frac{\partial}{\partial t} (\dot{\theta} \, v_L^2) - M_p (L + r_p) \int_0^L \frac{\partial}{\partial t} (\dot{\theta} \, v'^2) \, dx \\ &\quad + 2 M_p \, r_p \frac{\partial}{\partial t} (\dot{\theta} v_L v'_L) - M_p L r_p \frac{\partial}{\partial t} (\dot{\theta} v'^2_L) \end{aligned} \tag{5}$$

The equation associated with the link's deformation $v$ is:

$$\begin{aligned} 0 &= -\rho(\ddot{v} + x\,\ddot{\theta}) - EI_z v'''' + g\,\cos\theta\,(\rho[-v' + (L-x)v''] + M_p\,v'') - \rho\,g\sin\theta \\ &\quad +\dot{\theta}^2\left(\rho\,v + M_p[L+r_p]v'' + \frac{1}{2}\rho\left[-2x\,v' + (L^2-x^2)v''\right]\right) \end{aligned} \tag{6}$$

The BCs are given by:

$$\begin{aligned} 0 &= EI_z\,v'''\delta v\Big|_0^L - M_p(L\ddot{\theta} + \ddot{v}_L)\delta v_L - \frac{1}{2}\rho\dot{\theta}^2(L^2-x^2)v'\delta v\Big|_0^L + M_p\dot{\theta}^2 v_L\delta v_L \\ &\quad - M_p L\dot{\theta}^2 v'\delta v\Big|_0^L - \rho\,g\,\cos\theta(L-x)v'\delta v\Big|_0^L + M_p\,r_p\dot{\theta}^2 v'_L\delta v_L - M_p\,r_p\ddot{\theta}\delta v_L \\ &\quad -M_p\,r_p\ddot{v}'_L\delta v_L - M_p\,r_p\dot{\theta}^2 v'\,\delta v\Big|_0^L - M_p\,g\cos\theta v'\,\delta v\Big|_0^L - M_p\,g\sin\theta\delta v_L \end{aligned}$$

$$\begin{aligned} 0 &= -I_p(\ddot{\theta} + \ddot{v}'_L)\delta v'_L - EI_z\,v''\delta v'\Big|_0^L + M_p\,r_p\dot{\theta}^2 v_L\,\delta v'_L - M_p\,L\,r_p\ddot{\theta}\,\delta v'_L \\ &\quad -M_p\,r_p\ddot{v}_L\,\delta v'_L + M_p\,r_p^2\dot{\theta}^2 v'_L\,\delta v'_L - M_p\,r_p^2\ddot{\theta}\,\delta v'_L - M_p\,r_p^2\ddot{v}'_L\,\delta v'_L \\ &\quad -M_p\,r_p^2\dot{\theta}^2 v'_L\,\delta v'_L - M_p\,Lr_p\dot{\theta}^2 v'_L\,\delta v'_L - M_p\,r_p\,g\,\cos\theta v'_L\,\delta v'_L - M_p\,r_p\,g\,\sin\theta\,\delta v'_L \end{aligned}$$

To complete these dynamics, we add to the preceding equations the viscous friction at the base and the link's internal damping. To take into account the friction at the base in Eq. (5), the motor torque $T_m$ is replaced by $T_m - b_m\,\dot{\theta}$. The internal damping of the link is considered using the model of Voigt-Kelvin. This model gives the following relation between the constraint ($\sigma$) and the deformation ($\epsilon$):

$$\sigma = E(\epsilon + k_e\frac{d\epsilon}{dt})$$

In (6) and the associated BCs, Young modulus $E$ is replaced by:

$$E_k = E(1 + k_e D) \tag{7}$$

where $D$ is the partial derivatives operator, i.e. $Dv = \frac{\partial v}{\partial t}$.
Taking motor and internal damping into account, the dynamical equations (5)-(6) and the associated BCs are then replaced by:
**Dynamic Equation of the Motor's Angle $\theta$:**

$$\begin{aligned} T_m &= \left(I_m + \frac{1}{3}\rho\,L^3 + I_p + M_p(L+r_p)^2\right)\ddot{\theta} + b_m\dot{\theta} + \int_0^L \rho\,x\,\ddot{v}\,dx + M_p(L+r_p)\ddot{v}_L \\ &\quad +(I_p + M_p\,r_p(L+r_p))\ddot{v}'_L + \left(\frac{1}{2}\rho\,g\,L^2 + M_p\,g\,(L+r_p)\right)\sin\theta \\ &\quad + \left[\int_0^L \rho\,g\,v dx + M_p\,g\,(v_L + r_p\,v'_L)\right]\cos\theta + \int_0^L \frac{\partial}{\partial t}(\rho\dot{\theta}\,v^2)\,dx \\ &\quad -\frac{1}{2}\int_0^L \rho(L^2-x^2)\frac{\partial}{\partial t}(\dot{\theta}\,v'^2)\,dx + M_p\,\frac{\partial}{\partial t}(\dot{\theta}\,v_L^2) \\ &\quad -M_p(L+r_p)\int_0^L \frac{\partial}{\partial t}(\dot{\theta}\,v'^2)\,dx + 2M_p\,r_p\frac{\partial}{\partial t}(\dot{\theta}v_L v'_L) - M_p L r_p\frac{\partial}{\partial t}(\dot{\theta}v'^2_L) \end{aligned} \tag{8}$$

**Dynamic Equation of the Link's Deformation $v$:**

$$\begin{aligned} 0 &= -\rho(\ddot{v} + x\,\ddot{\theta}) - EI_z v'''' - k_e\, EI_z \dot{v}'''' + g\,\cos\theta\left(\rho[-v' + (L-x)v''] + M_p\, v''\right) - \rho\, g \sin\theta \\ &\quad + \dot{\theta}^2\left(\rho\, v + M_p[L + r_p]v'' + \frac{1}{2}\rho\left[-2x\, v' + (L^2 - x^2)v''\right]\right) \end{aligned} \tag{9}$$

**Boundary Conditions:**
The BCs are compatible with the geometric configuration of the given system. The link is clamped at the joint, i.e.

$$v(0,t) = v'(0,t) = 0,$$

and $\delta v(L,t)$ and $\delta v'(L,t)$ are arbitrary. The BCs are then given by:

$$\text{at } x = 0: \quad v_0 = 0 \text{ and } v_0' = 0 \tag{10}$$

at x=L:

$$\begin{aligned} E_k I_z\, v_L''' &= M_p(L\ddot{\theta} + \ddot{v}_L) + M_p\, r_p(\ddot{\theta} + \ddot{v}_L') - M_p\dot{\theta}^2(v_L + r_p\, v_L') + M_p(L + r_p)\dot{\theta}^2 v_L' \\ &\quad + M_p\, g\, v_L' \cos\theta + M_p\, g \sin\theta \end{aligned} \tag{11}$$

$$\begin{aligned} -E_k I_z\, v_L'' &= (I_p + M_p\, r_p^2)(\ddot{\theta} + \ddot{v}_L') + M_p\, r_p(L\ddot{\theta} + \ddot{v}_L) - M_p\, r_p(v_L + r_p\, v_L')\dot{\theta}^2 \\ &\quad + M_p\, r_p(L + r_p)v_L'\dot{\theta}^2 + M_p\, r_p\, g\, \cos\theta v_L' + M_p\, r_p\, g \sin\theta \end{aligned} \tag{12}$$

In the literature dynamics of flexible links manipulators with non linear kinematics were developed (Boyer et al., 2002; Piedboeuf, 1998). In (Boyer et al., 2002) the procedure of development of the dynamic equations of a robot with several flexible links is given. This procedure was applied to a robot having one flexible link. However, the analytical form of the model is not given.

## 3. Eigenvalues Problem

The eigenvalues problem (EVP) consists in solving, for deformation v, the dynamics of the system represented by ordinary differential equations (ODE) and partial differential equations (PDE) with associated BCs. Let us consider the case of a homogeneous problem where the motor's torque is null, i.e $T_m = 0$. We consider a solution for $v$ separable in space and time. The deformation is then given by:

$$v(x,t) = \phi(x) q_f(t) \tag{13}$$

where $\phi(x)$ represents the link's configuration and is only dependent on the spatial variable $x$, and $q_f(t)$ indicates the nature of the movement carried out by the configuration and depends only on time $t$. By substituting Eq. (13) in the dynamic equations and the associated BCs, the PDE associated with $v$ is transformed into ODE in $q_f(t)$. To have a stable solution, a harmonic movement is selected for $q_f(t)$ so that:

$$\ddot{q}_f(t) = -\omega^2 q_f(t)$$

where $\omega$ represents natural frequency of the system.
The EVP thus amounts finding one $\omega$ and a nontrivial solution $\phi(x)$ that verifies homogeneous discretized equations and the associated BCs. The corresponding $\omega$ are the characteristic values or the eigenvalues and the $\phi(x)$ are the eigenfunctions. EVP generally generates

the solution of a characteristic equation having an infinite countable solutions $w_r$. For each eigenvalue $w_r$ corresponds an eigenfunction $\phi_r(x)$. In the general case where dynamics is represented by nonlinear equations and with nonuniform parameters, a solution of the EVP is practically not possible. For that, we use approximate methods to solve this kind of problems.

## 4. Spatial Discretization

The order of the solution is infinite. In order to analyze and control this system, a spatially discrete model of finite order is suitable. A finite number is then retained in the discretization of the deformation which is rewritten in the form:

$$v(x,t) = \sum_{i=1}^{\nu} \phi_i(x)\, q_{f_i}(t) = \phi^T(x)\, q_f(t) \tag{14}$$

where $\nu$ is the number of retained modes, $\phi = [\phi_1,\ \phi_2,\ \ldots,\ \phi_\nu]^T$ et $q_f = [q_{f_1},\ q_{f_2},\ \ldots,\ q_{f_\nu}]^T$. The discretization of the kinetic energy (2) gives:

$$T = \frac{1}{2} I_t\, \dot{\theta}^2 + \dot{\theta} \beta^T \dot{q}_f + \frac{1}{2} \dot{q}_f^T\, M_{ff}\, \dot{q}_f + \frac{1}{2} \dot{\theta}^2 q_f^T\, C_{rr}\, q_f \tag{15}$$

where $I_t$ is the total inertia at the base, given by:

$$I_t = I_m + \frac{1}{3}\rho\, L^3 + I_p + M_p (L + r_p)^2$$

$$\beta = \int_0^L \rho\, x\, \phi\, dx + M_p (L + r_p)\phi_L + [I_p + M_p\, r_p (L + r_p)]\phi'_L$$

$$M_{ff} = \rho \int_0^L \phi\, \phi^T dx + M_p \phi_L\, \phi_L^T + (I_p + M_p\, r_p^2)\phi'_L\, \phi'^T_L + M_p\, r_p (\phi'_L\, \phi_L^T + \phi_L\, \phi'^T_L)$$

$$\begin{aligned} C_{rr} \;=\; & \rho \int_0^L \phi\, \phi^T\, dx + M_p\, \phi_L\, \phi_L^T + M_p\, r_p (\phi_L\, \phi'^T_L + \phi'_L\, \phi_L^T) - \rho \int_0^L x \int_0^x \phi'\, \phi'\, ds \\ & - M_p (L + r_p) \int_0^L \phi'\, \phi'^T\, dx - M_p\, r_p\, L \phi'_L\, \phi'^T_L \end{aligned}$$

In a matrix form,

$$T = \frac{1}{2} \underbrace{\begin{pmatrix} \dot{\theta} & \dot{q_f}^T \end{pmatrix}}_{\dot{q}^T} \underbrace{\begin{pmatrix} I_t + q_f^T\, C_{rr}\, q_f & \beta^T \\ \beta & M_{ff} \end{pmatrix}}_{M(q)} \underbrace{\begin{pmatrix} \dot{\theta} \\ \dot{q_f} \end{pmatrix}}_{\dot{q}} \tag{16}$$

The $q_f^T\, C_{rr}\, q_f$ element in the mass matrix $M(q)$ is of second order in $v$. It will be neglected. The potential energy (3) discretization gives:

$$\begin{aligned} V \;=\; & \frac{1}{2} q_f^T \int_0^L EI_z\, \phi''\, \phi''^T\, dx\, q_f - \left( \frac{1}{2} \rho\, g\, L^2 + M_p\, g (L + r_p) \right) \cos\theta \\ & + \frac{1}{2} g \cos\theta\, q_f^T \left( \rho \int_0^L \int_0^x \phi'\, \phi'^T\, ds dx + M_p \left[ \int_0^L \phi'\, \phi'^T\, dx + r_p\, \phi'_L\, \phi'^T_L \right] \right) q_f \\ & + g \sin\theta \left( \int_0^L \rho \phi^T\, dx + M_p (\phi_L^T + r_p\, \phi'^T_L) \right) q_f \\ \;=\; & \frac{1}{2} q_f^T\, K_{ff}\, q_f - G_{rr} \cos\theta + \frac{1}{2} \cos\theta\, q_f^T\, G_{ff}\, q_f + \sin\theta\, G_{rf}^T\, q_f \end{aligned} \tag{17}$$

where

$$\begin{aligned} K_{ff} &= EI_z \int_0^L \phi'' \, \phi''^T dx \\ G_{rr} &= \frac{1}{2}\rho\, g\, L^2 + M_p\, g(L + r_p) \\ G_{rf} &= \int_0^L \rho\, g\phi dx + M_p\, g(\phi_L + r_p \phi'_L) \\ G_{ff} &= \rho\, g \int_0^L (L - x)\phi' \phi'^T dx + M_p\, g \int_0^L \phi' \phi'^T dx + M_p\, g\, r_p\, \phi'_L\, \phi'^T_L \end{aligned}$$

The discretization of Rayleigh dissipation function (4) gives:

$$\begin{aligned} R &= \frac{1}{2} b_m \dot{q}_r^2 + \frac{1}{2} \dot{q}_f^T k_e \int_0^L EI_z \dot{v}''^2 \, dx \, \dot{q}_f \\ &= \frac{1}{2} \underbrace{\begin{pmatrix} \dot{\theta} & \dot{q_f}^T \end{pmatrix}}_{\dot{q}^T} \underbrace{\begin{pmatrix} b_m & 0 \\ 0 & B_{ff} \end{pmatrix}}_{B} \underbrace{\begin{pmatrix} \dot{\theta} \\ \dot{q_f} \end{pmatrix}}_{\dot{q}} \end{aligned} \tag{18}$$

where $B_{ff} = k_e K_{ff}$.
We then introduce these expressions into the Lagrangian $\mathcal{L} = T - V$, and we apply Lagrange equations,

$$\frac{d}{dt}\left(\frac{\partial \mathcal{L}}{\partial \dot{q}_j}\right) - \frac{\partial \mathcal{L}}{\partial q_j} + \frac{\partial R}{\partial \dot{q}_j} = Q_j, \quad j = 1,\, 2,\, \ldots,\, n \tag{19}$$

where $q_j$ is the generalized coordinates, $Q_j$ are the generalized forces, $j = 1,\, 2,\, \ldots,\, n$ and $n = \nu + 1$ is the total number of generalized coordinates. In Lagrange equations, $q_f(t)$ is the generalized coordinate vector associated with the flexibility. Let $q_r$ be the generalized coordinate associated with the base movement (rigid coordinate), i.e. $q_r(t) = \theta(t)$. The generalized coordinate vector is then given by:

$$q(t) = [q_r(t),\, q_f^T(t)]^T$$

The spatially discrete dynamical model is then given by:

$$T_m = I_t\, \ddot{q}_r + \beta^T \ddot{q}_f + b_m\, \dot{q}_r + G_{rr} \sin q_r + \cos q_r\, G_{rf}\, q_f + 2\dot{q}_r\, q_f^T\, C_{rr}\, \dot{q}_f + \ddot{q}_r\, q_f^T\, C_{rr} q_f \tag{20}$$

$$0 = \beta\, \ddot{q}_r + M_{ff}\, \ddot{q}_f + B_{ff}\dot{q}_f - \dot{q}_r^2\, C_{rr} q_f + K_{ff}\, q_f + g\, \cos q_r\, G_{ff}\, q_f + g \sin q_r\, G_{rf} \tag{21}$$

Written in a matrix form, equations (20)-(21) become:

$$\underbrace{\begin{pmatrix} I_t + q_f^T C_{rr} q_f & \beta^T \\ \beta & M_{ff} \end{pmatrix}}_{M(q)} \underbrace{\begin{pmatrix} \ddot{q}_r \\ \ddot{q}_f \end{pmatrix}}_{\ddot{q}} + \underbrace{\begin{pmatrix} b_m & 0 \\ 0 & B_{ff} \end{pmatrix}}_{B} \underbrace{\begin{pmatrix} \dot{q}_r \\ \dot{q}_f \end{pmatrix}}_{\dot{q}} + \underbrace{\begin{pmatrix} 0 & 0 \\ 0 & K_{ff} \end{pmatrix}}_{K} \underbrace{\begin{pmatrix} q_r \\ q_f \end{pmatrix}}_{q}$$

$$+ \underbrace{\underbrace{\begin{pmatrix} G_{rr} & G_{rf}^T \\ G_{rf} & G_{ff} \end{pmatrix}}_{G_1} \begin{pmatrix} \sin q_r \\ q_f \cos q_r \end{pmatrix}}_{G(q)} + \underbrace{\begin{pmatrix} 2\, \dot{q}_r\, q_f^T\, C_{rr}\, \dot{q}_f \\ -\dot{q}_r^2\, C_{rr}\, q_f \end{pmatrix}}_{C(q,\dot{q})\dot{q}} = \underbrace{\begin{pmatrix} 1 \\ 0 \end{pmatrix}}_{L} T_m \tag{22}$$

or also in the compact form:

$$M(q)\,\ddot{q} + C(q,\dot{q})\,\dot{q} + B\,\dot{q} + K\,q + G(q) = L\,T_m \tag{23}$$

where $M$, $B$, and $K$ are respectively the mass, damping, and rigidity matrices, and $C(q,\dot{q})\dot{q}$, and $G(q)$ are the Coriolis and centrifugal, and gravity force vectors.
$M$, $B$ and $K_{ff}$ are positive definite symmetric matrices. The associated matrix with the gravity, $G_1$, is also symmetric.

**Proposition 1.** *The mass matrix, M, and the Coriolis and centrifugal force vector, $C(q,\,\dot{q})\,\dot{q}$, verify the following:*

$$\dot{M}(q) - 2\,C(q,\,\dot{q}) = S \tag{24}$$

*where S is an antisymmetric matrix.*

**Proof**. Let

$$C(q,\,\dot{q}) = \begin{pmatrix} q_f^T C_{rr}\dot{q}_f & \dot{q}_r q_f^T C_{rr} \\ -\dot{q}_r C_{rr} q_f & 0 \end{pmatrix} \tag{25}$$

Then,

$$x^T\left(\dot{M}(q) - 2\,C(q,\,\dot{q})\right)x = 0 \quad \forall x \in \mathcal{R}^{(\nu+1)}$$

where $\nu$ is the flexible modes number, and $\mathcal{R}$ is the real set numbers. ▽
By neglecting the 2nd order elements (relative to $v$) in (23), i.e. in the mass matrix and the gravity element $G_{ff}$, (23) becomes:

$$M\,\ddot{q} + C(q,\dot{q})\,\dot{q} + B\,\dot{q} + K\,q + G(q) = L\,T_m \tag{26}$$

## 5. Description of Admissible Functions

In this section, we describe two types of admissible functions, namely, global functions defined over the entire beam length (such as beam eigenfunctions and polynomial functions) and piecewise polynomial functions (such as cubic splines and cubic B-splines).

### 5.1 Global Admissible Functions

#### 5.1.1 Beam Eigenfunctions

The analytical solution of the eigenfunctions of the system shown in Figure 1 are given by (Saad et al., 2006):

$$\phi_i(x) = A_i\left(\mu_3\lambda_i^3\left(\cos\beta_i x - \cosh\beta_i x\right) + (1+c_i)\sin\beta_i x + (1-c_i)\sinh\beta_i x - 2\beta_i x\right) \tag{27}$$

Here, $\beta_i = \frac{\lambda_i}{l}$ and $\lambda_i$ is the solution of the following characteristic equation :

$$\begin{aligned}\left(\mu_1\mu_2\mu_3 + \mu_2\mu_3\mu_5 - \mu_3\mu_4^2\right)\lambda^7\left(1 - C\,Ch\right) - \mu_3\left(\mu_1+\mu_5\right)\lambda^6\left(S\,Ch + C\,Sh\right) - 2\mu_3\mu_4\lambda^5 S\,Sh \\ + \left(\mu_2\mu_5 + \mu_1\mu_2 + \mu_2\mu_3 - \mu_4^2\right)\lambda^4\left(C\,Sh - S\,Ch\right) + \mu_3\lambda^3\left(1 + C\,Ch\right) + 2\left(\mu_1+\mu_5\right)\lambda^3 C\,Ch \\ +2\mu_4\lambda^2\left(C\,Sh + S\,Ch\right) + 2\mu_2\lambda S\,Sh + S\,Ch - C\,Sh = 0\end{aligned} \tag{28}$$

where:

$$\mu_1 = \frac{I_p}{\rho l^3},\ \mu_2 = \frac{m_p}{\rho l},\ \mu_3 = \frac{I_m}{\rho l^3},\ \mu_4 = \frac{m_p r_p}{\rho l^2},\ \mu_5 = \frac{m_p r_p^2}{\rho l^3},$$

$$C = \cos\lambda, \quad S = \sin\lambda, \quad Ch = \cosh\lambda, \quad Sh = \sinh\lambda.$$

The admissible shape functions are generally the eigenfunctions of a simpler but related problem. The eigenfunctions of a rotating beam with a payload concentrated at its end are obtained from (27) and (28) by replacing the payload center of mass $r_p$ by zero. The eigenfunctions of a clamped beam with or without payload are deduced by taking the motor inertia $I_m$ as infinity, or the payload inertia $I_p$ and mass $m_p$ as zero, respectively. The first four eigenfunctions of a rotating beam are shown in Figure 2.

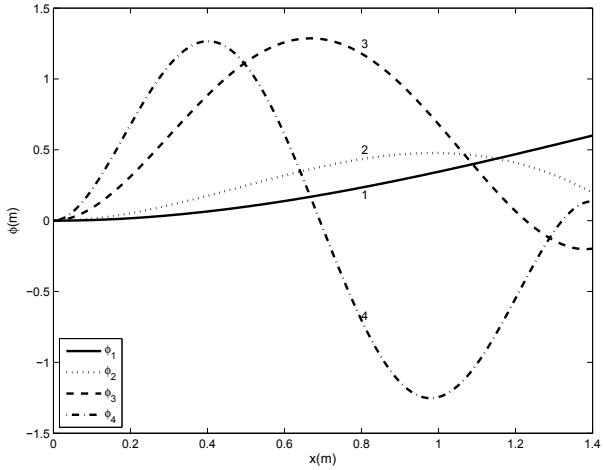


Fig. 2. First four eigenfunctions of a rotating beam

### 5.1.2 Polynomial functions

In this case, the beam deformation is given by

$$v(x,t) = \sum_{i=1}^{\nu} \left(\frac{x}{l}\right)^{i+1} \eta_i(t), \tag{29}$$

where, the BCs at $x = 0$ ($v_0 = v_0' = 0$) are considered. The vector of the assumed-modes is

$$\boldsymbol{\phi}^T(x) = \left[\left(\frac{x}{l}\right)^2 \ \cdots \ \left(\frac{x}{l}\right)^{i+1} \ \cdots \ \left(\frac{x}{l}\right)^{\nu} \ \left(\frac{x}{l}\right)^{\nu+1}\right]. \tag{30}$$

The polynomial functions are very simple. Figure 3 shows the first four polynomial functions. It is known that the sets of polynomial functions and beam eigenfunctions are complete, i.e., the error between the actual and the estimated eigenvalues can be rendered as small as desired by increasing the number of terms in the series (14) (Mirovitch, 1967). Therefore, the computed eigenvalues approach the actual ones from above as the number of admissible functions is increased.

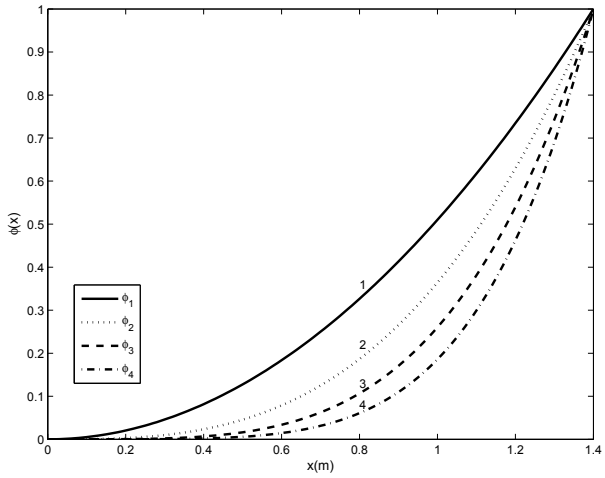


Fig. 3. First four polynomial functions

### 5.2 Piecewise admissible functions

The cubic splines and cubic B-splines are used as interpolation functions. In earlier studies, cubic splines were used in modeling specific types of robot manipulators by adjusting the BCs at both extremities (Cho et al., 1991). It is shown next that the cubic splines can be used simply as a set of assumed-modes by fixing the conditions at the link extremity, $x = l$, independently of the payload.

#### 5.2.1 Description of the cubic splines

On the interval $x_i <= x < x_{i+1}$, the deformation is approximated by a cubic spline function as (Gerald & Wheatley, 2004)

$$v_i(x,t) = a_i(x - x_i)^3 + b_i(x - x_i)^2 + c_i(x - x_i) + d_i. \tag{31}$$

The deformation $v$ and the curvature $v''$ at $x = x_i$ are $y_i$ and $y_i''$. The deformation and the curvature at $x = x_{i+1}$ are $y_{i+1}$ and $y_{i+1}''$. The continuity of the deformation and the curvature at the internal nodes gives the following relations:

$$\begin{aligned} a_i &= \frac{y_{i+1}'' - y_i''}{6h_i}, \\ b_i &= \frac{y_i''}{2}, \\ c_i &= \frac{y_{i+1} - y_i}{h_i} - \frac{2h_i\, y_i'' + h_i\, y_{i+1}''}{6}, \\ d_i &= y_i, \end{aligned}$$

where $h_i = x_{i+1} - x_i$. The continuity condition of the slope at $x = x_i$ ($v_i'(x_i, t) = v_{i-1}'(x_i, t)$) gives the following equation:

$$h_{i-1}\, y_{i-1}'' + 2(h_{i-1} + h_i)\, y_i'' + h_i\, y_{i+1}'' = 6\left(\frac{y_{i+1} - y_i}{h_i} - \frac{y_i - y_{i-1}}{h_{i-1}}\right). \tag{32}$$

Equation (32) is applicable to each of the internal nodes, from $i = 2$ to $n - 1$, where $n$ is the total number of nodes. This gives $n - 2$ equations relating the $n$ values of $y_i''$ and $y_i$. Two additional equations are obtained by specifying the conditions at both extremities. If the beam is assumed to be clamped into the base, then $v(0, t) = y_1 = 0$ and $v'(0, t) = 0$. It follows that:

$$2h_1\, y_1'' + h_1\, y_2'' = 6\,\frac{y_2}{h_1}. \tag{33}$$

For the distal extremity $x = l$, the conditions are to some extent arbitrary. Four choices are possible:

1. Taking $y_n'' = 0$, which amounts to assuming no bending moment;
2. Taking $y_n'' = y_{n-1}''$, which is equivalent to a constant bending moment on the last element;
3. Taking $y_n''$ as a linear extrapolation from $y_{n-1}''$ and $y_{n-2}''$ which yields

$$y_n'' = \frac{(h_{n-2} + h_{n-1})\, y_{n-1}'' - h_{n-1}\, y_{n-2}''}{h_{n-2}};$$

4. Keeping the curvature $y_n''$ at $x = l$ as an unknown. This choice is only applicable when the curvatures are taken as general coordinates as shown later.

An interesting feature of the cubic splines is the relation between the node curvatures and displacements. Indeed, combining (32) with the conditions for the extremities gives the following equation:

$$\mathbf{A}\mathbf{Y}'' = 6\mathbf{C}\mathbf{Y} \tag{34}$$

where, $\mathbf{Y}''$ and $\mathbf{Y}$ are the vectors of node curvatures and displacements. Equation (34) can be solved either for the displacement $\mathbf{Y}$ or the curvature $\mathbf{Y}''$. Therefore, the generalized coordinates used in the discrete model can be either the node curvatures or the node displacements. The use of curvatures presents some advantages in controlling flexible manipulators since these are directly measurable using strain gauges.

For a flexible link that is part of a general manipulator, the load at the link extremity is not known a priori. Therefore, the bending moment, which is related to the curvature, is unknown. When (34) is solved in terms of the node displacement $\mathbf{Y}$, the curvature at $x = l$ may remain unknown (condition 4 above). It means that the $n - 1$ displacements $y_i$ are expressed in terms of the $n$ curvatures $y_i''$.

An additional manipulation is required to put the cubic splines in a form suitable for the assumed-modes. A cubic spline is defined on each individual interval. To obtain the deformation $v$ at any point $x$ between 0 and $l$, the Heaviside function $\mu(x)$ is used ($\mu(x) = 1$ when $x \geq 0$ and $\mu(x) = 0$ when $x < 0$). The deformation $v$ is thus written as

$$v(x, t) = \sum_{i=1}^{n-1} v_i\,(\mu(x - x_i) - \mu(x - x_{i+1})) + v_{n-1}\,\mu(x - x_{n-1}). \tag{35}$$

It is then possible to express (35) in terms of the generalized flexible coordinates $\boldsymbol{\eta}$ (either the node displacements or curvatures) as follows:

$$\begin{aligned} v(x,t) &= \underbrace{\left(\frac{\partial v(x,t)}{\partial \mathbf{Y}''(t)}\right)^T}_{\boldsymbol{\phi}^T(x)} \underbrace{\mathbf{Y}''(t)}_{\boldsymbol{\eta}(t)} \quad \text{or} \\ v(x,t) &= \underbrace{\left(\frac{\partial v(x,t)}{\partial \mathbf{Y}(t)}\right)^T}_{\boldsymbol{\phi}^T(x)} \underbrace{\mathbf{Y}(t)}_{\boldsymbol{\eta}(t)}, \end{aligned} \tag{36}$$

where each component of the vector $\boldsymbol{\phi}(x)$ is an assumed-mode function $\boldsymbol{\phi}_i(x)$.
As an example, two cases are presented to illustrate the application of the cubic splines. The system used is the flexible rotating beam shown in Figure 1 where the link is divided into three finite elements. In the first case, the second condition ($Y_4'' = Y_3''$) is used to represent the curvature at the link extremity. Equation (34) becomes

$$\begin{aligned} &\underbrace{\begin{bmatrix} 2h_1 & h_1 & 0 \\ h_1 & 2(h_1+h_2) & h_2 \\ 0 & h_2 & 2h_2+3h_3 \end{bmatrix}}_{\mathbf{A}} \underbrace{\begin{bmatrix} y_1'' \\ y_2'' \\ y_3'' \end{bmatrix}}_{\mathbf{Y}''} \\ &= 6 \underbrace{\begin{bmatrix} \frac{1}{h_1} & 0 & 0 \\ -\frac{1}{h_1}-\frac{1}{h_2} & \frac{1}{h_2} & 0 \\ \frac{1}{h_2} & -\frac{1}{h_2}-\frac{1}{h_3} & \frac{1}{h_3} \end{bmatrix}}_{\mathbf{C}} \underbrace{\begin{bmatrix} y_2 \\ y_3 \\ y_4 \end{bmatrix}}_{\mathbf{Y}}. \end{aligned} \tag{37}$$

This equation can be solved either for the node curvatures $\mathbf{Y}''$ or for the node displacements $\mathbf{Y}$. If, in the second case, the curvature at the extremity, $Y_4''$, is left as an unknown, then the matrix $\mathbf{C}$ remains as in (37), while the matrix $\mathbf{A}$ becomes

$$\mathbf{A} = \begin{bmatrix} 2h_1 & h_1 & 0 & 0 \\ h_1 & 2(h_1+h_2) & h_2 & 0 \\ 0 & h_2 & 2(h_2+h_3) & h_3 \end{bmatrix}. \tag{38}$$

Equation (37) can only be solved for the node displacements while the node curvatures are the generalized coordinates.
Figure 4a illustrates the three assumed-modes when the node displacements are used as coordinates. Figure 4b shows the four assumed-modes when the node curvatures are used as coordinates while the curvature at the last node $y_4''$ is kept unknown.
The cubic interpolation functions verify the completeness and the continuity requirements for convergence. Therefore, one should expect that the solution of the resulting eigenvalue problem is, in the limit as $h \to 0$, convergent. However, monotonic convergence cannot be guaranteed. This is because two coordinates, displacement and curvature, are added for each element with each mesh refinement. Indeed, Mirovitch and Silverberg (1983) proposed two bracketing theorems characterizing the non-monotonic convergence of the eigensolution of the h-version of the FEM using Hermite cubics. It is shown in (Saad, 2004) that the eigensolution for the h-version of the FEM using cubic splines is monotonically convergent.

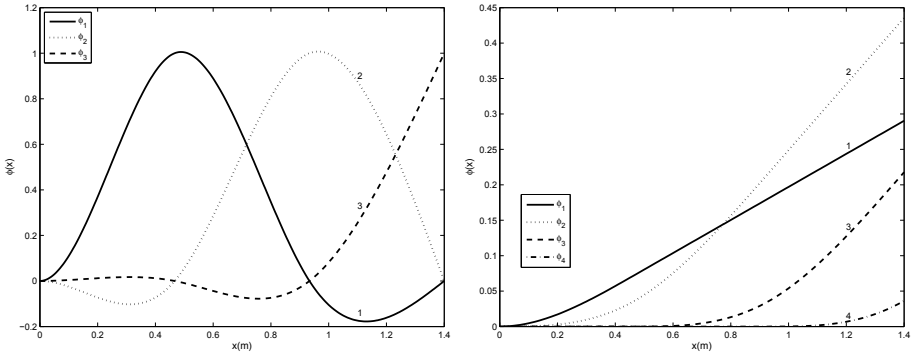


(a) Node displacements (b) Node curvatures

Fig. 4. Cubic splines defined on three intervals

#### 5.2.2 Description of the cubic B-splines

The cubic B-splines are used as interpolation functions in the Rayleigh-Ritz method and as assumed modes for flexible manipulators (Yang & Gibson, 1989). A cubic B-spline is defined on four intervals with a cubic spline on each interval as follows:

$$S_i(x) = a_i(x - x_i)^3 + b_i(x - x_i)^2 + c_i(x - x_i) + d_i, \tag{39}$$

for $x_{i-1} <= x < x_i$, $i = 1, \ldots, 4$. Since each cubic spline requires four parameters, a total of 16 parameters are needed. If the B-splines are different from zero on each interval, then continuity of the splines and their first two derivatives yields nine separate conditions. Six out of the remaining seven conditions can be found by fixing the three BCs at each extremity (namely $v$, $v'$, and $v''$). The last condition can be fixed arbitrarily at the middle node, e.g., by specifying unit displacement. A cubic B-spline can be zero on some of the four intervals.
For $n$ intervals, the required number $N$ of cubic B-splines is given by the following equation:

$$N = n - \nu_0 - \nu_1 + 3, \tag{40}$$

where, $\nu_0$ and $\nu_1$ are the numbers of BCs for $S(x)$, $S'(x)$ or $S''(x)$ being equal to zero at $x = 0$ and at $x = l$. For example, a beam clamped into a base and having a payload at its extremity has two zero BCs at $x = 0$ ($S(0) = S'(0) = 0$) and none at $x = l$. Therefore, $\nu_0 = 2$ and $\nu_1 = 0$. If the beam is divided into two intervals ($n = 2$), then three cubic B-splines are required.
As an example, we develop next a cubic B-spline defined on two intervals. The internal and BCs are:

$$\begin{gathered} S(x) = S'(x) = S''(x) = S'''(x) = 0 \text{ for } x_0 <= x < x_1, \\ S(x_1) = S'(x_1) = 0, \\ S(x),\ S'(x),\ S''(x) \text{ are continuous at } x = x_2, \\ \text{and } S(x_2) = 1, \\ S(x_3) = S''(x_3) = 0, \\ S(x) = S'(x) = S''(x) = S'''(x) = 0 \text{ for } x_3 <= x < x_4. \end{gathered}$$

It can be verified that 16 conditions are imposed. The Heaviside function is again used to insure that the functions are defined over the entire beam length. The B-spline verifying the above conditions is

$$\begin{aligned}\phi(x) = &\left(\frac{-11\,x^3 + 51\,x^2 - 69\,x + 29}{7}\right)\mu(x-1)\\ &+\left(\frac{16\,x^3 - 96\,x^2 + 192\,x - 128}{7}\right)\mu(x-2)\\ &+\left(\frac{-5\,x^3 + 45\,x^2 - 123\,x + 99}{7}\right)\mu(x-3).\end{aligned} \tag{41}$$

The choice of the B-splines must respect the geometric BCs. If any dynamic BC is zero, e.g., no inertial load, then taking this into account in the B-splines improves the solution convergence. Figure 5 shows the four cubic B-splines chosen as assumed modes when three intervals are used.

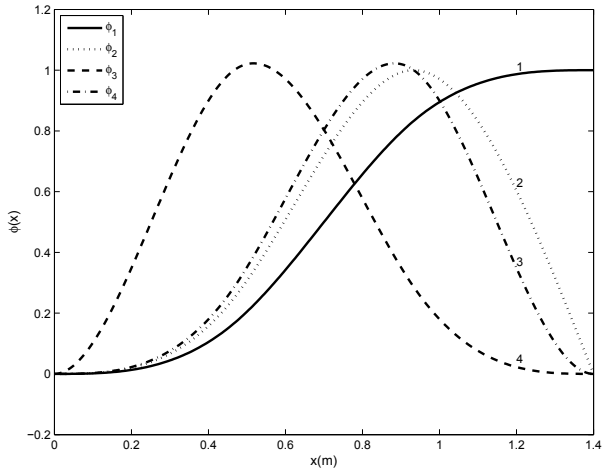


Fig. 5. Four cubic B-spline functions

## 6. Modal Analysis

The goal of this section is to study the accuracy of the different shape functions based models discussed in this paper in modeling the one-link robot system shown in Figure 1. First, a comparison in the frequency domain is carried out for frequencies, mode shapes and spatial derivative of mode shapes. Then, we compare the static mode shapes and their spatial derivatives (for $\theta = \pi/2$ as defined in the model assumptions). We also discuss the computational complexity to generate these functions.

Table 2 describes the shape functions used in the comparison. The determination of the beam eigenfunctions requires the knowledge of the system parameters. We are using the nominal parameters in these cases. On the other hand, the spline and polynomial shape functions require only the knowledge of the beam length. Still, for the cubic spline functions, we have

to make a choice for the BCs at the extremity. For the cubic B-splines, when there are less than four intervals, different B-splines can satisfy the geometric BCs (Saad et al., 2006).

| | |
|---|---|
| *cf* | Eigenfunctions of a clamped-free beam using the nominal parameters |
| *cp* | Eigenfunctions of a clamped-payload beam using the nominal parameters |
| *bp* | Eigenfunctions of a rotating beam using the nominal parameters |
| *cbs* | Cubic B-splines |
| *cs-d* | Cubic splines with displacements as coordinates and with the curvature at the last node $n$ being equal to the curvature at node $n-1$ |
| *cs-c* | Cubic splines with curvatures as coordinates and the curvature at the last node is kept unknown |
| *pol* | Polynomial functions |

Table 2. Shape functions used in the model comparison

To test the robustness of the shape functions given in Table 2, we vary the system parameters as presented in Table 3. In Case 1, the payload is removed. In Case 2, the motor inertia is reduced by a factor of one thousand. This is equivalent to removing a 32:1 reduction gear. In Case 3, the payload mass and inertia are increased by factors of 2.5 and 2.8 respectively. Additionally, the payload center of mass is moved further from the base to a position equivalent to 50% of the beam length. This provides insight into the more general two-link problem as the payload may be viewed as a rigid, locked, second link.

| Parameter | Nominal | Case 1 | Case 2 | Case 3 |
|---|---|---|---|---|
| $I_m\ (kg\,m^2)$ | 10 | 10 | 0.01 | 10 |
| $m_p\ (kg)$ | 2 | 0 | 2 | 5 |
| $I_p\ (kg\,m^2)$ | 0.36 | 0 | 0.36 | 1 |
| $r_p\ (m)$ | 0 | 0 | 0 | 0.7 |

Table 3. Variation of the nominal parameters

### 6.1 Performance indices for comparison

For each case, we compute the exact solution for the frequency comparison using the eigenfunctions of the rotating beam given by (27) and (28). For the static comparison, we compute the exact static deformation of a horizontal clamped-payload beam, by solving equations (9)-(12) with null time variations, which leads to:

$$s(x) = -\frac{g\,x^2}{24\,E\,I_z} \times \Big(\rho(x^2 - 4\,x\,l + 6\,l^2) + m_p(12\,l + 12\,r_p - 4\,x)\Big) \tag{42}$$

and get the estimated solutions using the spatially discretized model (23). The eigenfrequencies and eigenvectors are the solution of the following algebraic eigenvalue problem:

$$\mathbf{K}\mathbf{u} = \tilde{\omega}^2\mathbf{M}\mathbf{u}, \tag{43}$$

where, $\mathbf{M}$ and $\mathbf{K}$ are the mass and the stiffness matrices given in (23), $\tilde{\omega}$ is the estimated frequency, and $\mathbf{u}$ is the eigenvector associated with that frequency. Since damping is negligible, the rigid mode is always zero. It will not be included in the comparison results. We combine the eigenvectors corresponding to the flexible coordinates $\boldsymbol{\eta}$ in the following matrix:

$$\mathbf{U}_f = [\mathbf{u}_1 \ \cdots \ \mathbf{u}_\nu],$$

where $\nu$ is the number of the generalized coordinates. The following equation gives the eigenmodes or mode shapes in terms of the eigenvectors:

$$\tilde{Y}(x) = \mathbf{U}_f^T \boldsymbol{\phi}(x), \tag{44}$$

with $\boldsymbol{\phi}(x)$ the vector of shape functions. The first three derivatives of the mode shapes are computed using $\boldsymbol{\phi}'(x)$, $\boldsymbol{\phi}''(x)$ and $\boldsymbol{\phi}'''(x)$. The modes and their first derivatives are normalized such that their maximum is equal to one. The second and the third mode derivatives are normalized to equal one at $x = 0$.
We compute the relative error between the exact and the estimated frequencies using the following expression:

$$\epsilon_{f,i} = 100 \frac{\tilde{f}_i - f_i}{f_i}, \tag{45}$$

with $\tilde{f}_i$ and $f_i$ the approximate and the exact values of the $i$th frequency in $Hz$.
To compare the mode shapes, we use the average of the absolute error divided by the average of the absolute value of the exact mode shape:

$$\epsilon_{m_d,i} = 100 \frac{\int_0^l |\tilde{Y}_{d,i}(x) - Y_{d,i}(x)| dx}{\int_0^l |Y_{d,i}(x)| dx}, \tag{46}$$

where $d = 0, \ldots, 3$ denotes the mode shape derivative and $i$ is the mode number. $\tilde{Y}$ and $Y$ are the approximated and the exact mode shapes.
The estimated static deformation is evaluated using (14) and (23) as follows:

$$\tilde{s}(x) = \boldsymbol{\phi}(x)^T \mathbf{K}_{ff}^{-1} \mathbf{h}_f. \tag{47}$$

The first three derivatives of the static mode shapes are obtained using $\boldsymbol{\phi}'(x)$, $\boldsymbol{\phi}''(x)$ and $\boldsymbol{\phi}'''(x)$. The error is similar to the one calculated for the mode shapes and is given by

$$\epsilon_{s_d,i} = 100 \frac{\int_0^l |\tilde{s}_{d,i}(x) - s_d(x)| dx}{\int_0^l |s_d(x)| dx}. \tag{48}$$

### 6.2 Comparison results

For each of the shape functions given in Table 2, we generated models using one to eight shape functions (2 to 8 for the Splines) for each of the four cases for a total of 212 different models. These models are created with Maple using the symbolic modeling programs SYMOFROS (Piedboeuf, 1996) and the analysis is done using MATLAB. For all studied cases, the exact frequencies are generated symbolically and computed numerically in MAPLE with a 30 digits precision to avoid truncation in Matlab. In this paper, we study the improvement in the solution when using one to eight shape functions. We are presenting only the results for the first three modes but the discussion applies to higher modes as well.

### 6.2.1 Non-Concentrated Payload (Case 3)

Since Case 3 is the most challenging one, we discuss it in more details. Figure 6 gives the absolute eigenvalue relative errors in (45) for the shape functions presented in Table 2. The exact frequencies for the first three modes are 1.6, 9.3 and 45.3 Hz. On each graph, three curves appear for each shape function. The lowest one corresponds to the first mode and the highest one to the third mode. For example, three *cs-c* shape functions give an error of 0.05% on the second frequency (Figure 6b). The graphs show the solution improvement when the number of shape functions increases. The curves for *bp* and *cp* models are very close, especially for the second and third modes (Figure 6a). For the first frequency, the precision of *cp* and *bp* models does not improve after three shape functions owing to numerical errors. The curves for *cbs* and *cs-c* models are almost identical for the three modes. The *cp* and *bp* models give smaller errors for the first and second modes than the *cbs* and *cs-c* models but not for the third mode (Figure 6a vs. 6b). The error for the *cf* model barely goes under 1% (Figure 6a). The error for the *cs-d* first mode is higher than the second mode error of the *cs-c* model (Figure 6b). For the first mode, the *pol* model gives results similar to the *cbs* model up to five shape functions: the results are even identical when two shape functions are used (Figure 6c). Afterward, the precision diminishes drastically mainly because the powers $(\frac{x}{l})^k$ are nearly linearly dependent since they essentially have the same weight in the neighborhood of $x = l$.

Figure 7 shows the relative errors on the eigenmodes while Figure 8 gives the error on the second derivatives. The second derivative is important in experimentation since it is related to the curvature read by strain-gauges. The observations done for the frequencies hold for the eigenmodes and their second derivative. However, the error on the eigenmode approximation is higher than the one on the frequencies. The error on the second derivative is even higher. For example, the error on the first mode of the *cf* model for the second derivative (Figure 8a) goes barely under 10% even with eight shape functions. The errors on the *pol* model for the second derivative sometime increase when a shape function is added (Figure 8c). The error on the eigenmodes for the *pol* model are close to *cbs* and *cs-c* models up to four shape functions.

Figure 9 shows the static shape errors while Figure 10 gives the errors on the second derivative of the static shape functions. Clearly, the *pol* model gives the best result, especially for three shape functions. This was expected since the exact solution (Equation 42) is a fourth order polynomial. The *cp* , *bp* , *cbs* and *cs-c* models have similar errors (*cbs* and *cs-c* are even superimposed). The error for the *cf* model is important especially for the second derivative where the lowest error is around 6% with eight shape functions. The *cs-d* model does not perform as well as the two others spline models (*cbs* and *cs-c* ).

### 6.2.2 Nominal, No-Payload (Case 1) and Reduced Inertia (Case 2)

Globally, the above observations for decentralized payload (Case 3) hold also for the Nominal, the No-Payload (Case 1), and for Reduced Inertia (Case 2) cases. In particular, for the Nominal Case, as expected the *bp* model gives the best results. It represents the exact solution of the system at hand. The eigenfrequencies and eigenmodes errors are due to numerical errors since the exact frequencies are computed symbolically in MAPLE with a 30 digits precision. The behavior of the other models are generally the same as for Case 3. Still, the convergence rate of the *cp* model is better in Case 3. Additionally, the error on the first frequency for the *cs-c* model is higher in Case 3. The case with no payload (Case 1) is the only one where the *cf* model gives good results. The other models that do not assume a zero bending torque at the extremity take longer to converge and the errors are larger than those in Case 3. For the

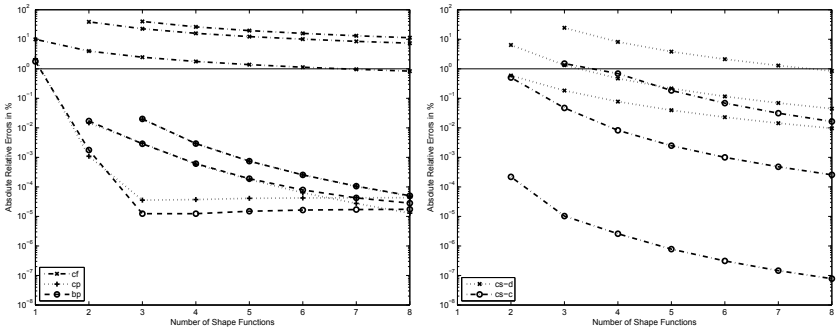


(a) *cf*, *cp* and *bp* models (b) *cs-d* and *cs-c* models

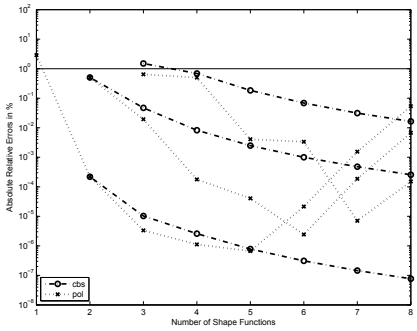


(c) *cbs* and *pol* models

Fig. 6. Absolute relative errors on the eigenvalues in % for Case 3

spline models, it will be easy to generate a spline having zero moment at the extremity. Such splines improve the results. When the base inertia is reduced by a factor of 1000 (Case 2), the convergence rate of the selected parameters is slower and more shape functions are required to reach the same precision as compared to Case 3.

#### 6.2.3 Sensitivity of the models

Table 4 gives the condition number of the eigenvector matrix, $CN_2(V)$ (Watkins, 1991), of the different models, from one to eight shape functions. These condition numbers measure the sensitivity of the eigenvalues to the system parameter variations. They indicate by how much a variation in the $\mathbf{M}^{-1}\mathbf{K}$ matrix will be amplified (a condition number of one being the best case). Table 4 reveals that the *pol* model becomes very sensitive when more shape functions are added. Therefore, while the solution should improve by adding shape functions, the sensitivity to numerical and parameter errors wipes off this improvement. The sensitivity of the *cf* and *cs-d* models and, to a less extent, of *cbs* model also increases when the number of shape functions increases. On the other hand, the sensitivities of the *cp* , *bp* and *cs-c* models stay almost constant. The *cs-c* model with the lowest condition number is then the less sensitive to model error.

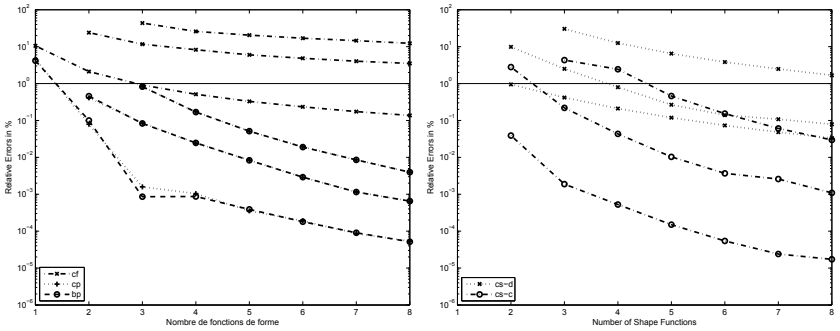


(a) *cf*, *cp* and *bp* models (b) *cs-c* and *cs-d* models

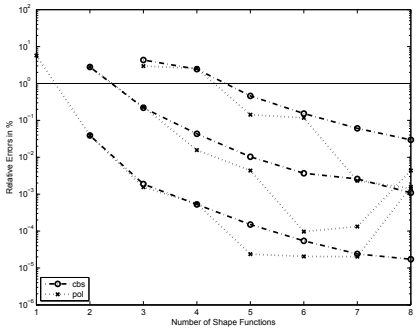


(c) *cbs* and *pol* models

Fig. 7. Relative errors on the eigenmodes in % for Case 3

## 7. Conclusion

In this work, the mathematical model of a flexible link manipulator using the assumed-mode method to discretize the link flexibility was presented. A detailed comparison of several admissible shape functions in assumed-mode models was carried out on a flexible slewing beam for the eigenvalues, the eigenmodes and their derivatives, and the static deformations and their derivatives. Load parameters were changed from their nominal values to test the sensitivity of the shape functions based models. The study confirms the fact that the completeness of the admissible functions guarantees convergence of the approximate models but the convergence rate can be slow. In clamped-free case, it was revealed that the poor convergence is related to the inability of satisfying the natural BCs with a finite number of assumed-modes. The comparisons show that for the system of a one flexible link: (1) the clamped-free eigenfunctions are mostly inadequate. They only behave well when there is no payload; (2) the clamped-payload eigenfunctions are good candidates even when the payload parameters are changed; (3) in comparison to the clamped-payload eigenfunctions, the complexity of the rotating beam eigenfunctions did not translate into marked rate convergence improvement; (4) the polynomial functions are very attractive and are generally good for a small number of shape functions, but they are too sensitive to system parameters variations; (5) both the cu-

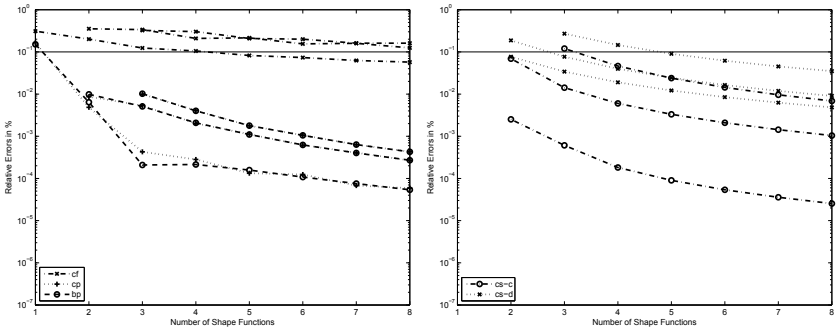


(a) *cf*, *cp* and *bp* models (b) *cs-c* and *cs-d* models

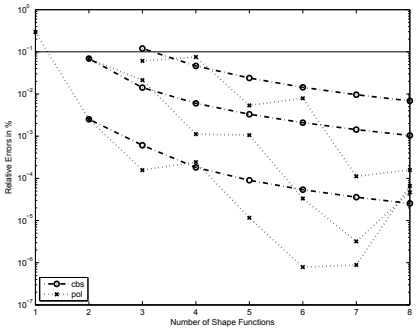


(c) *cbs* and *pol* models

Fig. 8. Relative errors on the 2nd derivative of the eigenmodes in % for Case 3

bic B-splines and the cubic splines with curvatures as coordinates offer identical behavior; (6) the cubic splines with curvatures as coordinates provides better results than the cubic splines with displacements as coordinates for all the convergence criteria; (7) overall, the cubic splines using curvatures as generalized coordinates offer the best compromise between good precision and low calculation complexity. It is also worth to mention that based on the results of this paper, the cubic spline functions are now utilized in Symofros in the discretization of the deformation of Canada Flexible Arm at the Space Canadian Agency rather than the beam eigenfunctions or the polynomial functions that were previously used.

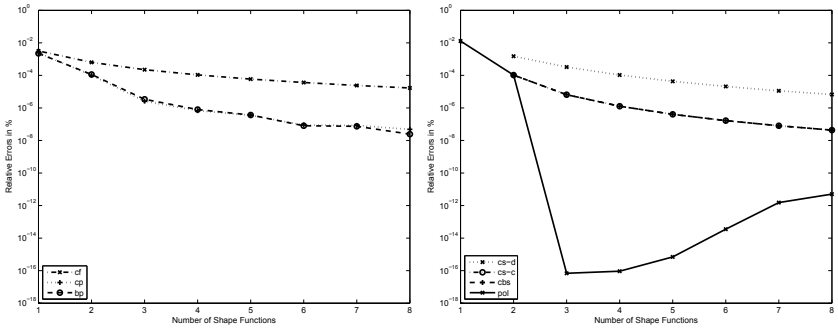


(a) *cf*, *cp* and *bp* models (b) *cs-c*, *cs-d* , *cbs* , and *pol* models

Fig. 9. Relative errors on the static shapes in % for Case 3

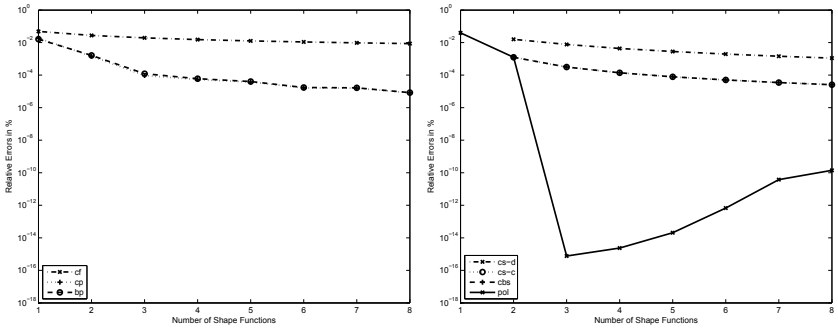


(a) *cf*, *cp* and *bp* models (b) *cs-c*, *cs-d* , *cbs* , and *pol* models

Fig. 10. Relative errors on the 2nd derivative of the static shape in % for Case 3

| | 1 | 2 | 3 | 4 | 5 | 6 | 7 | 8 |
|---|---|---|---|---|---|---|---|---|
| *cf* | 2.3 | 6.1 | 10.7 | 16.1 | 22.3 | 29.2 | 36.6 | 44.7 |
| *cp* | 1.4 | 2.5 | 2.5 | 2.5 | 2.5 | 2.5 | 2.5 | 2.5 |
| *bp* | 1.5 | 2.2 | 2.2 | 2.2 | 2.2 | 2.2 | 2.2 | 2.2 |
| *cbs* | – | 2.3 | 4.9 | 3.6 | 4.8 | 6.2 | 7.7 | 9.3 |
| *cs-c* | – | 1.7 | 1.7 | 1.7 | 1.6 | 1.6 | 1.6 | 1.6 |
| *cs-d* | – | 5.2 | 8.4 | 12.1 | 16.3 | 21.1 | 26.2 | 31.6 |
| *pol* | 1.9 | 4.8 | 11.6 | 24.4 | 54.5 | 253 | 1.3e3 | 7.3e3 |

Table 4. Condition number on the eigenvalue matrix for Case 3

## 8. References

Barbieri, E. and Özguner, U. (1988). Unconstrained and Constrained Mode Expansions for a Flexible Slewing Link, *ASME Journal of Dynamic Systems, Measurement, and Control*, Vol. 110, No. 4, 416–421.

Book, W. and Obergfell, K. (2000). Practical Models for Practical Flexible Arms, *Proc. 2000 IEEE International Conference on Robotics and Automation*, San Francisco, CA, April, 835–842.

F. Boyer, N. Glandais, and W. Khalil, (2002). Flexible Multibody Dynamics Based on a Non-Linear Euler-Bernoulli Kinematics. *International Journal for Numerical Methods in Engineering*, Vol. 54, No. 1, 27-59.

Buffinton, K.W. and Lam, J. (1992). A Comparative Study of Simple Dynamic Models and Control Schemes for Elastic Manipulators, *American Control Conference*, Chicago, IL, USA, June, 3334–3339.

Cetinkunt, S. and Yu, S. (1991). Closed-Loop Behavior of a Feedback-Controlled Flexible Arm: A Comparative Study, *International Journal of Robotics Research*, Vol. 10, No. 3, 263–275.

Chen, C.H. and Menq, J.S. (1990). Experiments on the Payload-Adaptation of a Flexible One-Link Manipulator with Unknown Payload, *Proc. 1990 IEEE International Conference on Robotics and Automation*, Cincinnati, OH, USA, May, 1614–1619.

Cho, K. *et al*. (1991). On the Controllability and Observability of Flexible Beams Under Rigid-Body Motion, *IEEE International Conference on Industrial Eletronics, Control and Instrumentation (IECON'91)*, Kobe, Japan, 455–460.

Gerald, C.F. and Wheatley, P.O. (2004). *Applied Numerical Analysis*, Addison Wesley, Boston.

Hastings, G.G. and Book, W.J. (1987). A Linear Dynamic Model for Flexible Robotic Manipulator, *IEEE Control Systems Magazine*, Vol. 7, No. 1, 61–64.

Junkins, J.L. and Kim, Y. (1993). *Introduction to Dynamics and Control of Flexible Structure*, AIAA, Washington, D.C.

Li, D. *et al*. (1998). Dynamic Modeling and Mode Analysis of Flexible-Link, Flexible-Joint Robots, *Mechanism and Machine Theory*, Vol. 33, No. 7, 1031–1044.

Meirovitch, L. (1967). *Analytical Methods in Vibrations*, MacMillan, New York.

Meirovitch, L. and Silverberg, L.M. (1983). Two Bracketing Theorems Characterizing the Eigensolution for the *h*-Version of the Finite Element Method, *International Journal for Numerical Methods in Engineering*, Vol. 19, 1691–1704.

Meirovitch, L. and Kwak, M.K. (1990). Convergence of the Classical Rayleigh-Ritz Method and the Finite Element Method, *AIAA Journal*, Vol. 28, No. 8, 1509–1516.

Moallem, M., Patel, R.V., and Khorasani, K., (2002). Nonlinear Tip-Position Tracking Control of a Flexible- Link Manipulator: Theory and Experiments, *Automatica*, Vol. 37, No. 11, 1825–1834.

Nicosia, S., Valigi, P., and Zaccarian, L. (1996). Dynamic Modelling of a Two Link Flexible Robot Experimental Validation, *Proc. 1996 IEEE International Conference on Robotics and Automation*, Leuven, Belgium, April, 1953–1958.

Parks, T.R. and Pak, H.A. (1991). Effect of Payload on the Dynamics of a Flexible Manipulator - Modeling for Control, *ASME Journal of Dynamic Systems Measurment and Control*, Vol. 113, No. 3, 409–418.

Piedbœuf, J.C. (2001). Six Methods to Model a Flexible Beam Rotating in the Vertical Plane, *Proc. 2001 IEEE International Conference on Robotics and Automation*, Seoul, Korea, May, 2832–2839.

Piedbœuf, J.-C. (1996). Modeling of Flexible Robots with Maple, *The Maple Technical Newsletter*, Vol. 3, No. 1, 38–47.

J.-C. Piedbœuf, (1998). Recursive Modeling of Serial Flexible Manipulators, *Journal of the Astronautical Sciences*, Vol. 47, No. 1, 1-24.

Piedbœuf, J.-C. and Miller, S. (1994). Estimation of Endpoint Position and Orientation of a Flexible Link Using Strain Gauges, *4th IFAC Symposium on Robot Control*, Capri, Italy, September, 675–680.

Saad M. (2004). Modélisation et commande par la passivité d'un système à un bras flexible, *Ph.D. dissertation*, École Polytechnique de Montréal, Montréal, Canada.

Saad, M., Piedboeuf, J.-C., Akhrif, O, and Saydy, L. (2005). Modal analysis of assumed-mode models of a flexible slewing beam, *Int. J. Modelling, Identification and Control*, Vol. 1, No. 4, 325–337.

Saad, M., Akhrif, O, and Saydy, L. (2000). Robust Noncollocated Passive Models of a Flexible Link with Uncertain Payload and Joint Inertia, *7th IEEE International Conference on Electronics, Circuits and Systems*, Beirut, Lebanon, December, 713–717.

Stanway, J. *et al*. (1998). Comparison and Validation of Dynamics Simulation Models for a Structurally Flexible Manipulator, *ASME Journal of Dynamic Systems, Measurement, and Control*, Vol. 120, No. 3, 404–409.

Theodore, R. and Ghosal, A. (1995). Comparison of the Assumed Modes and Finite Element Models for Flexible Multilink Manipulators, *International Journal of Robotics Research*, Vol. 14, No. 2, 91–111.

Tokhi, M.O. and Mohamed, Z. (1999). Finite Element Approach to Dynamic Modelling of a Flexible Robot Manipulator: Performance Evaluation and Computational Requirements, *Communications in Numerical Methods in Engineering*, Vol. 15, No. 9, 669–678.

Watkins, D.S. (1991). *Fundamentals of Matrix Computations*, John Wiley, New York.

Xia, Z. and Menq, C.H. (1992). Modeling and Control of Flexible Manipulators: Part I - Dynamic Analysis and Characterization, *AMD, ASME, Dynamics of Flexible Multibody Systems: Theory and Experiment*, Vol. 141, 105–114.

Yang, Y.P. and Gibson, J.S. (1989). Adaptive control of a flexible manipulator with a flexible link, *Journal of Robotic Systems*, Vol. 6, No. 3, 217–232.

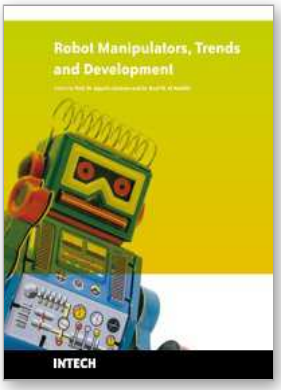


**Robot Manipulators Trends and Development**

Edited by Agustin Jimenez and Basil M Al Hadithi

ISBN 978-953-307-073-5
Hard cover, 666 pages
**Publisher** InTech
**Published online** 01, March, 2010
**Published in print edition** March, 2010

This book presents the most recent research advances in robot manipulators. It offers a complete survey to the kinematic and dynamic modelling, simulation, computer vision, software engineering, optimization and design of control algorithms applied for robotic systems. It is devoted for a large scale of applications, such as manufacturing, manipulation, medicine and automation. Several control methods are included such as optimal, adaptive, robust, force, fuzzy and neural network control strategies. The trajectory planning is discussed in details for point-to-point and path motions control. The results in obtained in this book are expected to be of great interest for researchers, engineers, scientists and students, in engineering studies and industrial sectors related to robot modelling, design, control, and application. The book also details theoretical, mathematical and practical requirements for mathematicians and control engineers. It surveys recent techniques in modelling, computer simulation and implementation of advanced and intelligent controllers.



**InTech Europe**
University Campus STeP Ri
Slavka Krautzeka 83/A
51000 Rijeka, Croatia
Phone: +385 (51) 770 447
Fax: +385 (51) 686 166
www.intechopen.com

**InTech China**
Unit 405, Office Block, Hotel Equatorial Shanghai
No.65, Yan An Road (West), Shanghai, 200040, China
中国上海市延安西路65号上海国际贵都大饭店办公楼405单元
Phone: +86-21-62489820
Fax: +86-21-62489821